International Journal for Modern Trends in Science and Technology
Volume 12, Issue 04, pages 684-694.
ISSN: 2455-3778 online
Available online at: http://www.ijmtst.com/vol12issue04.html
DOI: https://doi.org/10.5281/zenodo.19536631

Intelligent ANN-Based Control of Solar PV Integrated PMBLDC Motor Drive with Bidirectional Power Flow Management

A Naveen Reddy, Chennuri DinakarJohn, Dasari Raghu Vamsi, Y Durga Bhavani, D Phanikumar

Department of Electrical and Electronics Engineering, Vasireddy Venkatadri Institute of Technology, Pedakakani, Namburu, Guntur, India.

To Cite this Article
A Naveen Reddy, Chennuri DinakarJohn, Dasari Raghu Vamsi, Y Durga Bhavani & D Phanikumar (2026). Intelligent ANN-Based Control of Solar PV Integrated PMBLDC Motor Drive with Bidirectional Power Flow Management. International Journal for Modern Trends in Science and Technology, 12(04), 684-694. https://doi.org/10.5281/zenodo.19536631

Article Info
Received: 16 March 2026; Revised: 06 April 2026; Accepted: 10 April 2026.

KEYWORDS

Artificial Neural Network (ANN), Permanent Magnet Brushless DC (PMBLDC) Motor, Solar Photovoltaic (PV) System, Maximum Power Point Tracking (MPPT), Bidirectional DC–DC Converter, Energy Storage System.

ABSTRACT

This paper presents the design and analysis of an advanced control strategy for a Permanent Magnet Brushless DC (PMBLDC) motor drive powered by a renewable energy source. Unlike conventional systems that rely on proportional-integral (PI) and fuzzy logic controllers for speed regulation, the proposed method integrates a solar photovoltaic (PV) system with a Perturb and Observe (P&O) Maximum Power Point Tracking (MPPT) algorithm, a boost converter, and a battery energy storage unit connected through a bidirectional buck–boost converter. The solar MPPT-based boost converter ensures maximum power extraction under varying environmental conditions, while the bidirectional converter enables efficient energy management between the PV source, battery, and motor load. For speed control of the BLDC motor, an Artificial Neural Network (ANN) controller is employed, offering superior adaptability and learning capability compared to traditional controllers. The entire system is modeled and simulated in MATLAB/Simulink to evaluate its dynamic performance under different operating conditions. Simulation results demonstrate that the proposed ANN-based control scheme provides improved speed regulation, faster transient response, reduced steady-state error, and enhanced system efficiency compared to conventional PI and fuzzy logic controllers. Additionally, the integration of renewable energy and energy storage enhances system reliability and sustainability.

1. INTRODUCTION

The increasing demand for energy-efficient and environmentally sustainable systems has accelerated the integration of renewable energy sources into electric drive applications. Among various renewable sources, solar photovoltaic (PV) systems have gained significant attention due to their abundance, reliability, and ease of integration into standalone and grid-connected systems [1], [2]. In recent years, PV-powered motor drives have emerged as a promising solution for applications such as electric vehicles, water pumping, and industrial automation, offering reduced dependence on fossil fuels and lower carbon emissions [3], [4]. Permanent Magnet Brushless DC (PMBLDC) motors have become a preferred choice in modern drive systems due to their high efficiency, compact size, high torque-to-weight ratio, and low maintenance requirements [5], [6]. These motors are widely used in renewable energy-based applications because of their superior dynamic performance and compatibility with power electronic converters [7]. However, the performance of PMBLDC motor drives is highly dependent on the effectiveness of the control strategy employed for speed regulation and power management [8]. Conventional control techniques such as proportional–integral (PI) controllers are commonly used for motor speed control due to their simplicity and ease of implementation [9]. However, PI controllers often suffer from poor performance under nonlinear and time-varying conditions, especially in systems powered by renewable energy sources where fluctuations in input power are significant [10]. Fuzzy logic controllers have been proposed as an alternative to improve system performance under uncertain conditions; nevertheless, they require expert knowledge for rule design and may not always guarantee optimal performance [11], [12]. To overcome these limitations, Artificial Neural Network (ANN)-based control techniques have been widely explored in recent years. ANN controllers possess the ability to learn complex nonlinear relationships, adapt to changing operating conditions, and provide improved dynamic performance compared to traditional controllers [13], [14]. In motor drive applications, ANN-based speed controllers have demonstrated faster response, reduced steady-state error, and enhanced robustness against disturbances [15].

In PV-integrated systems, efficient power extraction is a critical requirement due to the intermittent nature of solar energy. Maximum Power Point Tracking (MPPT) techniques are employed to ensure that the PV system operates at its optimal power point under varying irradiance and temperature conditions [16]. Among various MPPT methods, the Perturb and Observe (P&O) algorithm is widely used due to its simplicity and ease of implementation [17]. The extracted power is typically regulated using DC–DC converters, such as boost converters, to match the voltage requirements of the load or storage system [18]. Energy storage systems play a vital role in enhancing the reliability and stability of renewable energy-based motor drives. The integration of battery energy storage allows the system to store excess energy during low load conditions and supply power during insufficient generation, thereby ensuring continuous operation [19], [20]. Bidirectional DC–DC converters are commonly used to facilitate energy exchange between the PV system, battery, and load, enabling efficient power flow management [21]. These converters support both charging and discharging modes, improving overall system flexibility and energy utilization [22]. Despite significant advancements, challenges remain in achieving efficient coordination among PV generation, energy storage, and motor load under dynamic operating conditions. Variations in solar irradiance, load demand, and battery state of charge can significantly impact system performance, requiring intelligent control strategies for optimal operation [23]. In this context, ANN-based controllers offer a promising solution by providing adaptive and intelligent control capabilities for both speed regulation and power management [24]. Therefore, this paper proposes an intelligent ANN-based control strategy for a solar PV integrated PMBLDC motor drive with bidirectional power flow management [25]. The system incorporates a P&O MPPT-based boost converter for maximum power extraction and a bidirectional buck–boost converter for efficient energy management between the PV source, battery, and motor load. The ANN controller is designed to regulate motor speed with improved dynamic performance under varying operating conditions. The effectiveness of the proposed approach is validated through MATLAB/Simulink simulations, demonstrating enhanced performance in terms of speed regulation,

transient response, and overall system efficiency compared to conventional control methods.

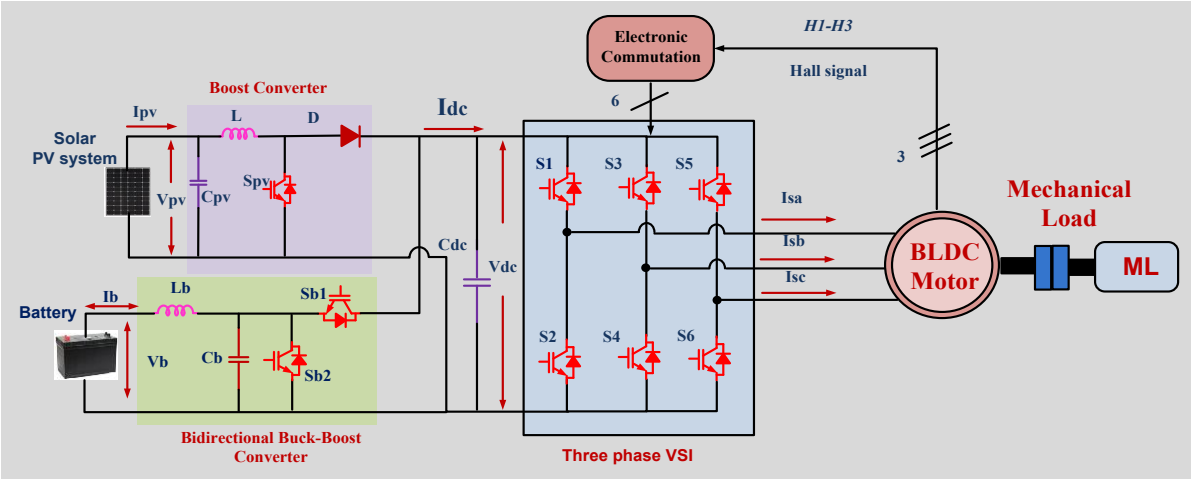

Fig. 1. Architecture of renewable based EVs charging station.

II. SYSTEM CONFIGURATION

The proposed system comprises a solar photovoltaic (PV)-integrated Permanent Magnet Brushless DC (PMBLDC) motor drive with bidirectional power flow capability as shown in Fig.1. The PV system acts as the primary energy source and is connected to the DC link through a boost converter. This converter is controlled using a Maximum Power Point Tracking (MPPT) algorithm to ensure maximum power extraction under varying solar irradiance conditions and to regulate the PV output voltage. A battery energy storage system is connected to the DC link via a bidirectional buck–boost converter. This converter enables controlled charging and discharging of the battery, allowing efficient energy exchange between the PV source, battery, and motor load. When PV generation exceeds load demand, excess energy is stored in the battery, whereas during low generation conditions, the battery supplies power to maintain continuous system operation. The DC link, supported by a capacitor, provides a stable voltage to a three-phase Voltage Source Inverter (VSI). The VSI converts DC power into three-phase AC supply required for driving the PMBLDC motor. The inverter switching is governed by electronic commutation using Hall sensor signals, which provide rotor position information for proper phase excitation. The PMBLDC motor is coupled to a mechanical load, and its speed is controlled using an ANN-based controller. The controller ensures improved dynamic response, reduced steady-state error, and reliable performance under varying operating conditions. Overall, the integrated system enables efficient power management, stable motor operation, and enhanced utilization of renewable energy.

III. MODELING AND DESIGNING OF PROPOSED SYSTEM

A. Solar Power System

The solar power system plays a crucial role in optimizing load management and system stability in grid-connected hybrid renewable energy systems (HRES). The integration of solar photovoltaic (PV) generation with electric vehicle (EV) charging infrastructure requires efficient maximum power extraction, voltage regulation, and power flow control. This section provides a detailed solar PV model, MPPT techniques, power converters, and

a. Solar PV System Modeling

A Photovoltaic (PV) system converts solar energy into electrical power using photovoltaic cells. The output power of a PV module depends on factors such as solar irradiance, temperature, and load conditions. The general mathematical model of a solar PV module is derived from the single-diode equivalent circuit and is expressed as:

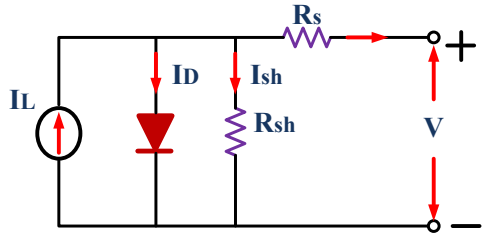

Fig. 2 equivalent model of PV solar.

$$I = I_{Ph} - I_o\left(e^{\frac{q(V+IR_S)}{nKT}} - 1\right) - \frac{V+IR_S}{R_{sh}} \quad (1)$$

Where:

- Iph = Photogenerated current (dependent on solar irradiance and temperature)
- Io = Reverse saturation current
- q = Electron charge (1.6×10^{-19} C)
- V = PV module output voltage
- I = PV module output current
- Rs = Series resistance of the PV cell
- Rsh = Shunt resistance of the PV cell
- n = Ideality factor of the diode
- K = Boltzmann's constant (1.38×10^{-23} J/K)
- T = Temperature in Kelvin

B. Solar PV Boost Converter with P&O MPPT Algorithm

A solar PV boost converter with a Perturb and Observe (P&O) MPPT algorithm is designed to maximize power extraction from a photovoltaic (PV) panel while ensuring the output voltage is suitable for the connected load or battery as shown in Fig.3. The PV panel generates DC electricity, but its output varies with irradiance and temperature, requiring an MPPT controller to operate at the Maximum Power Point (MPP). A boost converter, consisting of an inductor, MOSFET switch, diode, and capacitor, is used to step up the PV voltage. When the MOSFET switch is ON, the inductor stores energy from the PV panel, and when the MOSFET is OFF, the inductor releases energy to the output, thereby increasing the voltage.

The output voltage (Vo) is controlled by adjusting the duty cycle (D) using the relation

$$V_0 = V_{PV} / (1 - D) \quad (2)$$

The P&O MPPT algorithm works by continuously perturbing the PV voltage and observing the resulting power change. It first measures the PV voltage (Vpv) and current (Ipv), then calculates the power (Ppv). If a small increase in voltage leads to an increase in power, the algorithm continues perturbing in the same direction; otherwise, it reverses the perturbation to reach the MPP. This iterative process ensures that the PV panel operates at its highest efficiency. The combination of the boost converter and P&O MPPT controller effectively regulates the PV output, improving energy harvesting efficiency and providing a stable power supply for various applications.

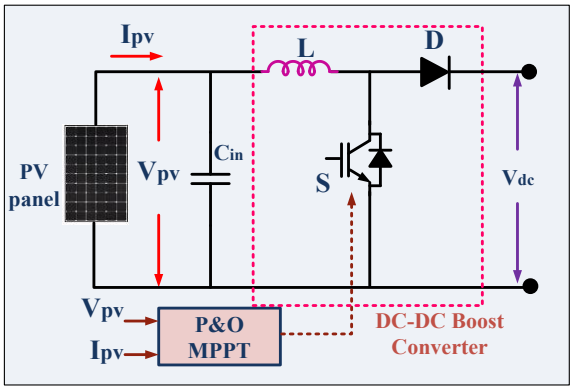

Fig. 3 solar PV P&O MPPT DC-DC boost converter

C. Perturb and Observe (P&O) MPPT Algorithm

The Perturb and Observe (P&O) Maximum Power Point Tracking (MPPT) algorithm is one of the most widely used techniques for optimizing the power output from a solar photovoltaic (PV) system. The power generated by a PV panel depends on environmental conditions such as solar irradiance and temperature, making it necessary to continuously track the Maximum Power Point (MPP) for efficient operation as shown in Fig.4. The P&O algorithm operates by making small perturbations (incremental changes) to the PV voltage (Vpv) and observing the resulting changes in power (Ppv). Based on this observation, the algorithm decides whether to continue perturbing in the same direction or to reverse the perturbation to ensure that the system remains near the MPP. The working can be summarized as follows:

1. Measure the PV voltage (Vpv) and current (Ipv), then compute the power:

$$P_{Pv} = V_{Pv} \times I_{Pv} \quad (3)$$

2. Compare the new power value with the previous power value (Ppv(n) and Ppv(n−1)):
   - If Ppv(n)>Ppv(n−1), it means the system is moving towards the MPP, so the voltage perturbation is maintained in the same direction.
   - If Ppv(n)<Ppv(n−1), it indicates that the system has moved away from the MPP, so the voltage perturbation direction is reversed.

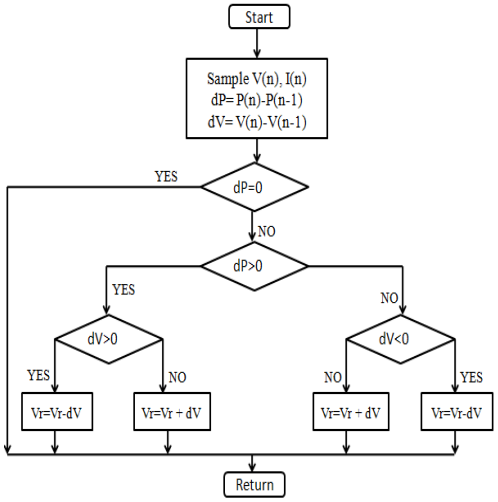

Fig. 4 flow chart of P&O MPPT algorithm

The process continues iteratively to keep the system at or near the maximum power point. The decision-making process of the P&O algorithm is expressed as:

$if\ dP_{Pv}/dV_{pv} > 0 \rightarrow increase\ v_{pv}$ (4)

$if\ dP_{Pv}/dV_{pv} < 0 \rightarrow decrease\ v_{pv}$ (5)

Where

$dP_{Pv} = P_{pv}(n) - p_{pv(n-1)}$ (6)

$dV_{Pv} = V_{pV}(n) - V_{pv(n-1)}$ (7)

The duty cycle (D) of the boost converter is adjusted accordingly to ensure the operating point moves toward the MPP. The duty cycle is updated as:

$D(n) = D(n-1) \pm \Delta D$ (8)

Where ΔD is the perturbation step size.

D. Bidirectional Buck-Boost Converter for Battery Energy Storage System

The bidirectional buck-boost converter plays a crucial role in managing energy flow between the battery energy storage system (BESS) and the DC bus in a microgrid. This converter enables both charging and discharging of the battery, ensuring stable power delivery for electric vehicle (EV) charging. In buck mode, the converter steps down the DC bus voltage to charge the battery, while in boost mode, it steps up the battery voltage to supply power to the microgrid or EV load as shown in Fig.5. The control strategy dynamically adjusts the duty cycle to regulate power flow efficiently. The converter also helps stabilize the DC bus voltage, mitigating fluctuations from intermittent renewable energy sources like solar and wind. The energy management strategy ensures optimal charging and discharging cycles, enhancing battery lifespan and overall system efficiency.

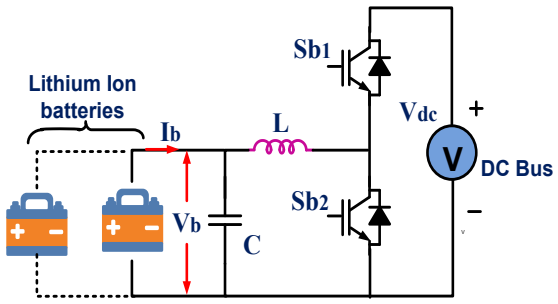

Fig.5 principle operation bidirectional dc-dc buck boost converter

1. Buck Mode (Battery Charging)

Output Voltage in Buck Mode:

$V_b = D \cdot V_{dc}$ (9)

Where: Vb = Battery voltage, Vdc = DC bus voltage, D = Duty cycle (0<D<1)

Inductor Current Ripple in Buck Mode:

$\Delta I_L = \frac{(1-D)V_{dc}}{Lf_S}$ (10)

Where: ΔIL = Inductor current ripple, L = Inductor value, fs = Switching frequency

2. Boost Mode (Battery Discharging)

Output Voltage in Boost Mode:

$V_{dc} = \frac{V_b}{1-D}$ (11)

Inductor Current Ripple in Boost Mode:

$\Delta I_L = \frac{DV_b}{Lf_S}$ (12)

E. Double-Loop Controller for EV Charging System

The control strategy for electric vehicle (EV) charging involves a double-loop control system to ensure efficient, stable, and safe charging as shown in Fig.6. The outer voltage loop maintains a constant DC bus voltage, while the inner current loop regulates the battery charging current. A Proportional-Integral (PI) controller is used in both loops to minimize steady-state error and improve dynamic performance.

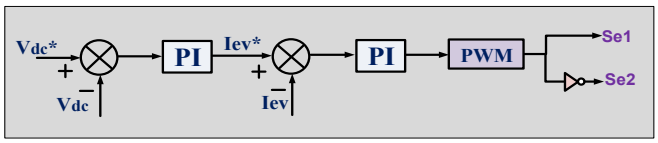

Fig. 6 double loop ev charging controller

1. Outer Voltage Loop: DC Bus Voltage Control

The outer voltage loop ensures the DC bus voltage (V_{dc}) remains stable and within the desired range. Since variations in EV charging loads and grid fluctuations affect the DC bus voltage, this loop provides a reference current (I_{ev}^*) for the inner current loop.

Error Signal Calculation:

$$e_v(t) = V_{dc}^* - V_{dC} \quad (13)$$

PI Controller Output (Reference EV Charging Current Iev∗

$$I_{ev}^*(t) = K_{Pv} e_v(t) + k_{iv} \int e_v(t)\, dt \quad (14)$$

Where: Iev∗= Reference charging current for the inner loop, Kpv= Proportional gain of voltage controller, Kiv= Integral gain of voltage controller

This reference current is then passed to the inner current loop for precise battery charging control.

2. Inner Current Loop: Battery Current Control

The inner current loop ensures the EV battery is charged with a smooth and regulated current to prevent over current issues and battery degradation. The PI controller in this loop generates the duty cycle for the DC-DC converter (buck or boost).

Error Signal Calculation:

$$e_i(t) = I_{ev}^* - I_{ev} \quad (15)$$

PI Controller Output (Duty Cycle Control)

$$D(t) = K_{Pi} e_i(t) + k_{ii} \int e_i(t)\, dt \quad (16)$$

Where: D = Duty cycle of the DC-DC converter, Kpi= Proportional gain of current controller, Kii= Integral gain of current controller

This duty cycle (D) is applied to the DC-DC converter, adjusting the output voltage and current to regulate battery charging.

IV. Modeling and Designing of BLDC motor

The Brushless DC (BLDC) motor is modeled and designed based on the principles of electromagnetic torque generation using electronically commutated stator windings. Unlike conventional DC motors, the BLDC motor does not use brushes for commutation; instead, it employs a three-phase inverter and rotor position sensors, such as Hall-effect sensors, for precise control of the switching sequence. The motor is designed with a permanent magnet rotor and stator windings arranged in a trapezoidal back-EMF configuration to ensure efficient torque production with minimal torque ripple. The mathematical model of the BLDC motor consists of dynamic equations for stator voltage, current, back EMF, and torque generation, implemented in the MATLAB/Simulink environment. The inverter used to drive the motor is controlled based on the rotor position feedback, allowing real-time commutation and speed regulation. Parameters such as stator resistance, inductance, and the back EMF constant are carefully selected to match the application requirements. The simulation model incorporates a closed-loop control system that adjusts the motor speed according to the desired set point while maintaining stable operation even under varying load conditions. This modeling approach enables accurate analysis of motor dynamics, efficiency, and performance in the smart energy system.

A. Mathematical Designing of BLDC Motor

The Brushless DC (BLDC) motor is designed using a set of mathematical equations that describe its electrical and mechanical behavior. The BLDC motor consists of a three-phase stator and a permanent magnet rotor. Unlike brushed DC motors, commutation in a BLDC motor is performed electronically through a three-phase inverter, which is controlled based on the rotor position sensed by Hall-effect sensors.

The stator winding of the BLDC motor follows the basic form of the phase voltage equation, which for each phase can be written as:

$$V_a = R \cdot i_a + L \cdot \frac{di_a}{dt} + e_a \quad (17)$$

$$V_b = R \cdot i_b + L \cdot \frac{di_b}{dt} + e_b \quad (18)$$

$$V_c = R \cdot i_c + L \cdot \frac{di_c}{dt} + e_c \quad (19)$$

Where: Va,Vb,Vc are the phase voltages, ia,ib,ic are the phase currents, R is the stator resistance per phase, L is the stator inductance per phase, ea,eb,ec are the back electromotive forces (EMF) of each phase

The back-EMF in each phase is dependent on the rotor position and speed, and is expressed as:

$$e_a = f_a(\theta) \cdot \omega \cdot k_e \quad (20)$$

$$e_b = f_b(\theta) \cdot \omega \cdot k_e \quad (21)$$

$$e_c = f_c(\theta) \cdot \omega \cdot k_e \quad (22)$$

Where: fa(θ),fb(θ),fc(θ) are the trapezoidal back-EMF waveforms as a function of rotor position θ, ω is the rotor speed in rad/s, Ke is the back-EMF constant

The electromagnetic torque generated by the motor is given by:

$$T_a = \frac{1}{\omega}(e_a i_a + e_b i_b + e_c i_c) \quad (23)$$

The mechanical equation of the motor governing its rotational dynamics is:

$$T_e - T_L = J \cdot \frac{d\omega}{dt} + B \cdot \omega \quad (24)$$

Where: TL is the load torque, J is the moment of inertia, B is the damping coefficient

The motor is typically controlled using a six-step (trapezoidal) commutation technique where each pair of inverter switches conducts for 120° electrical duration. Hall-effect sensors or sensorless estimation techniques

are used to determine rotor position and enable appropriate switching sequences in the inverter.

V. Designing of ANN Controller for Speed Control of BLDC Motor

The ANN controller is designed to regulate the speed of the BLDC motor by approximating the nonlinear control law between the speed error signals and the required control action. In the proposed system, the ANN replaces the conventional controller and generates the reference control signal for the voltage source inverter so that the actual motor speed closely follows the desired reference speed. The controller processes the speed error and change in speed error through multiple network layers, where each layer performs weighted summation followed by a nonlinear activation function. This improves tracking performance, reduces steady-state error, and enhances transient response under varying load and source conditions.

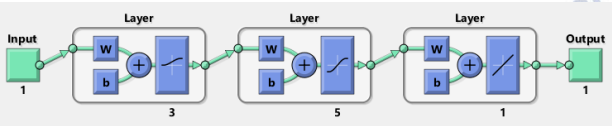

Figure 7: Structure of Neural Network

A. Actual Speed Measurement and Error Calculation

The ANN controller input is derived from the difference between the reference speed and the measured motor speed. The instantaneous speed error is expressed as

$$e(t) = \omega^*(t) - \omega(t) \quad (25)$$

where ω∗(t) is the reference speed of the BLDC motor, ω(t) is the actual measured motor speed, and e(t) is the instantaneous speed error.

The change in error is also considered as an additional input in order to capture the dynamic variation of the speed response:

$$\Delta e(t) = e(t) - e(t-1) \quad (26)$$

Hence, the ANN input vector is written as

$$x(t) = \begin{bmatrix} e(t) \\ \Delta e(t) \end{bmatrix} \quad (27)$$

This allows the controller to use both the present deviation and the trend of speed variation to predict the appropriate control action.

B. General ANN Mapping

The ANN approximates the nonlinear mapping between the input vector and the control output as

$$u(t) = f_{ANN}(x(t), w, b) \quad (28)$$

where u(t) is the control output of the ANN, x(t) is the input vector, W and b represent the weight matrices and bias vectors, and fANN denotes the nonlinear mapping realized by the network. For BLDC motor speed control, the ANN output u(t) may be taken as the reference current, duty ratio, or control voltage for the VSI, depending on the implementation. In this work, it is used to produce the control signal required to regulate inverter operation and maintain the desired motor speed.

C. Input to First Hidden Layer

Each neuron in the first hidden layer performs weighted summation of the inputs:

$$z_1 = W_1 x(t) + b_1 \quad (29)$$

where W1 is the weight matrix connecting the input layer to the first hidden layer and b1 is the corresponding bias vector.

The activation function used in the first hidden layer is the log-sigmoid function:

$$h_1 = f_1(z_1) = \log\text{sig}(z_1) = \frac{1}{1+e^{-z_1}} \quad (30)$$

The log-sigmoid function compresses the neuron output into the range [0,1], which is useful for smooth nonlinear mapping and normalized internal representation.

D. First Hidden Layer to Second Hidden Layer

The outputs of the first hidden layer are then combined in the second hidden layer according to

$$z_2 = W_2 h_1 + b_2 \quad (31)$$

The activation function in the second hidden layer is the tangent-sigmoid function:

$$h_2 = f_2(z_2) = \tan\text{sig}(z_2) = \frac{2}{1+e^{-2z_2}} - 1 \quad (32)$$

which is equivalent to the hyperbolic tangent function:

$$\tanh(z) = \frac{e^z - e^{-z}}{e^z + e^{-z}} \quad (33)$$

The tansig activation function produces outputs in the range [−1,+1]. Its symmetry about zero makes it suitable for representing both accelerating and decelerating control actions in BLDC motor speed regulation.

E. Output Layer

The output layer performs a linear combination of the second hidden layer outputs:

$$z_3 = W_3 h_2 + b_3 \quad (34)$$

A linear activation function is employed at the output layer:

$$u(t) = f_3(z_3) = purelin(z_3) = z_3 \quad (35)$$

This allows the ANN to generate an unbounded continuous control signal suitable for the inverter or motor drive controller.

F. Training Objective

The ANN parameters are adjusted by minimizing the mean squared error between the target control signal and the ANN output. The performance index is defined as

$$E = \frac{1}{N}\sum_{k=1}^{N}[T(k) - n(k)]^2 \quad (36)$$

where T(k) is the target control signal, u(k) is the ANN output, and NNN is the total number of training samples. For BLDC speed control, the training data are generated from the motor drive under different operating conditions, including changes in speed reference, load torque, and DC-link voltage. Thus, the ANN learns the appropriate control action needed to maintain stable speed tracking.

E. Weight Update Rule

The network weights are updated using the Levenberg–Marquardt learning algorithm, expressed as

$$W^{new} = W^{old} - (J^T J + uI)^{-1} J^T e \quad (37)$$

where J is the Jacobian matrix of the error function, e is the error vector between the ANN output and the target output, μ is the learning parameter, and III is the identity matrix. This training method provides fast convergence and improved stability during offline learning.

F. Closed-Loop ANN Speed Controller

After training, the ANN is incorporated into the closed-loop speed control system of the BLDC motor as

$$\omega^*(t) \rightarrow [e(t), \Delta e(t)] \rightarrow ANN \rightarrow u(t) \rightarrow VSL/ BLDCMotor \rightarrow \omega(t) \quad (38)$$

where ω∗(t) is the reference speed, [e(t), Δe(t)] are the ANN inputs, u(t) is the control output generated by the network, and ω(t) is the actual motor speed.

In this configuration, the ANN continuously adjusts the control signal according to the speed tracking error, thereby ensuring fast dynamic response, minimum overshoot, reduced steady-state error, and improved robustness against supply and load disturbances.

G. BLDC Motor Speed Dynamics

The mechanical dynamics of the BLDC motor can be represented by

$$T_e - T_L = J\frac{d\omega}{dt} + B\omega \quad (39)$$

where Te is the electromagnetic torque, TL is the load torque, J is the moment of inertia, B is the viscous friction coefficient, and ω is the rotor speed.

The electromagnetic torque is proportional to the phase current and is given by

$$T_e = K_t i \quad (40)$$

where Kt is the torque constant and i is the motor current. By controlling the inverter switching through the ANN-generated signal, the motor current and developed torque are regulated, which in turn controls the rotor speed.

VI. RESULTS AND DISCUSSION

A. Performance Evaluation and Discussion of the Proposed System

The results obtained from the simulation illustrate the dynamic behavior of the photovoltaic (PV) system under a disturbance or change in operating conditions as shown in Fig.8. Initially, from time 0 to 0.5 seconds, the PV voltage (Vpv) remains almost constant at around 300 V, indicating that the system is operating in a stable steady-state condition. This stability suggests that the PV array is likely functioning near its optimal operating point, possibly under maximum power point tracking (MPPT) control, where both irradiance and load conditions are constant. The absence of significant fluctuations in this region confirms that the converter and control strategy are effectively maintaining a regulated output. However, at around 0.5 seconds, a sudden and significant drop in the PV voltage is observed, decreasing sharply from approximately 300 V to about 150 V. This abrupt change indicates the occurrence of a disturbance, which could be due to several factors such as a step change in load, a variation in solar irradiance, or a modification in the duty cycle of the DC-DC converter. Following this drop, the voltage does not immediately stabilize but instead continues to gradually decline, eventually settling in the range of 120–130 V. This gradual decrease suggests that the system is undergoing a transient adjustment period as it attempts to reach a new equilibrium point. The final stabilized voltage being lower than the initial value implies that the system has transitioned to a different operating region, possibly away from the original maximum power point. The current waveform (Ib) further supports this interpretation of system dynamics. Before 0.6 seconds, the current exhibits high-frequency oscillations with relatively small amplitude, which is characteristic of switching behavior in power electronic converters. These oscillations are typically caused by the pulse-width modulation (PWM) switching of semiconductor devices and indicate normal converter operation. The current appears to be centered around a small average value, suggesting balanced energy transfer under steady conditions. At 0.6 seconds, shortly after the voltage disturbance, the current waveform shows

pronounced transient spikes, with peaks reaching as high as 30–35 A. These spikes represent the system's immediate response to the sudden voltage drop and reflect a surge in current as the converter attempts to compensate for the change. Such behavior is typical in power electronic systems when there is a rapid shift in operating conditions, leading to temporary overshoots due to energy storage elements like inductors and capacitors. Following this transient event, the current waveform becomes less dense in terms of switching frequency and shows reduced oscillatory behavior, indicating that the system is stabilizing. The amplitude of the current also appears to decrease and settle into a new steady-state pattern, corresponding to the lower voltage level observed in the PV output. This suggests that the control system has successfully adapted to the new operating condition, albeit at a different equilibrium point. Overall, the results demonstrate that the system responds dynamically to disturbances, exhibiting a clear transient phase characterized by voltage drops and current spikes, followed by a gradual stabilization. The interaction between the PV source, the DC-DC converter, and the control mechanism is evident in both the voltage and current responses. While the system ultimately achieves stability, the presence of significant transients indicates that there may be room for improvement in the control strategy to reduce overshoot and enhance response time. These findings highlight the importance of robust control design in maintaining optimal performance and minimizing the impact of disturbances in PV-based power systems.

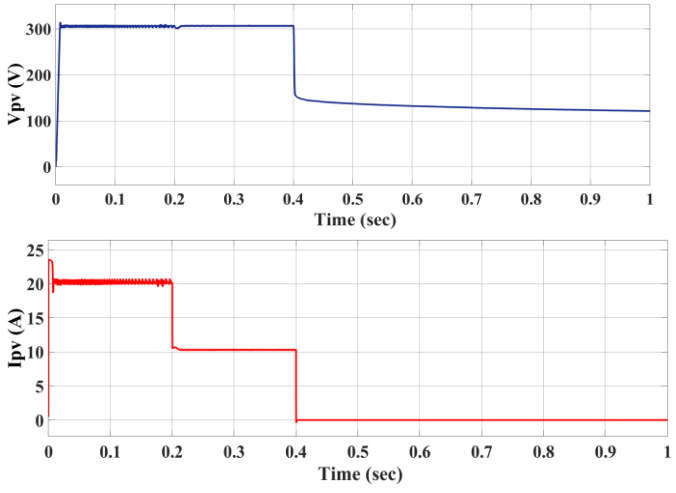

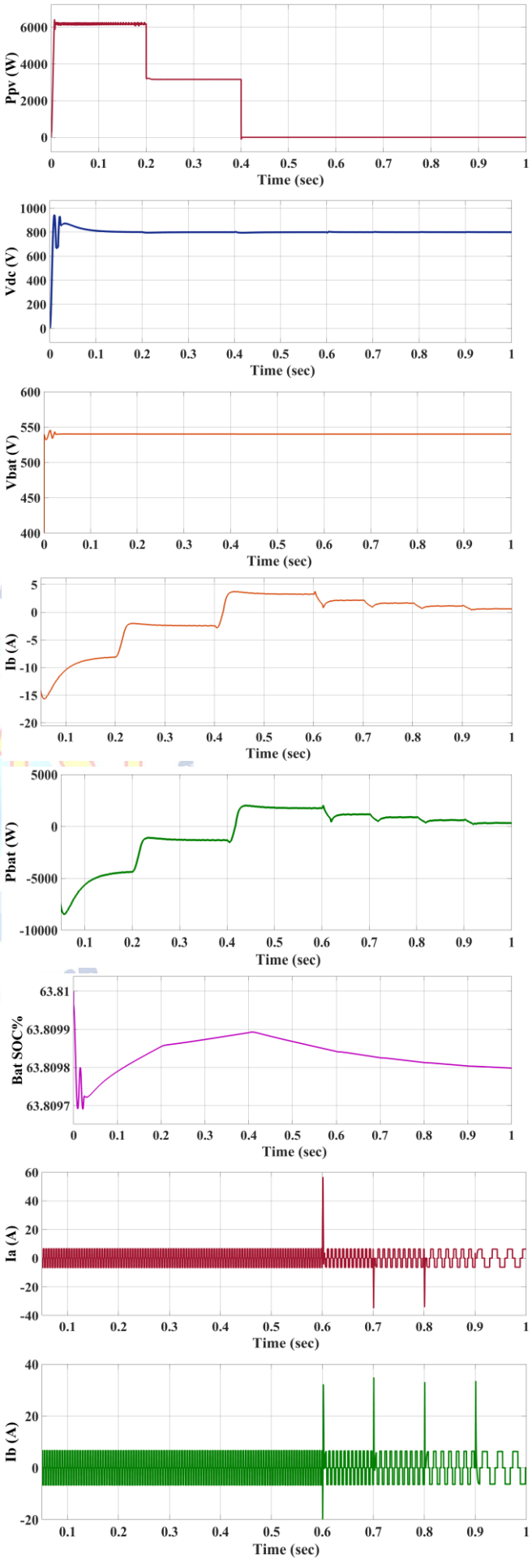

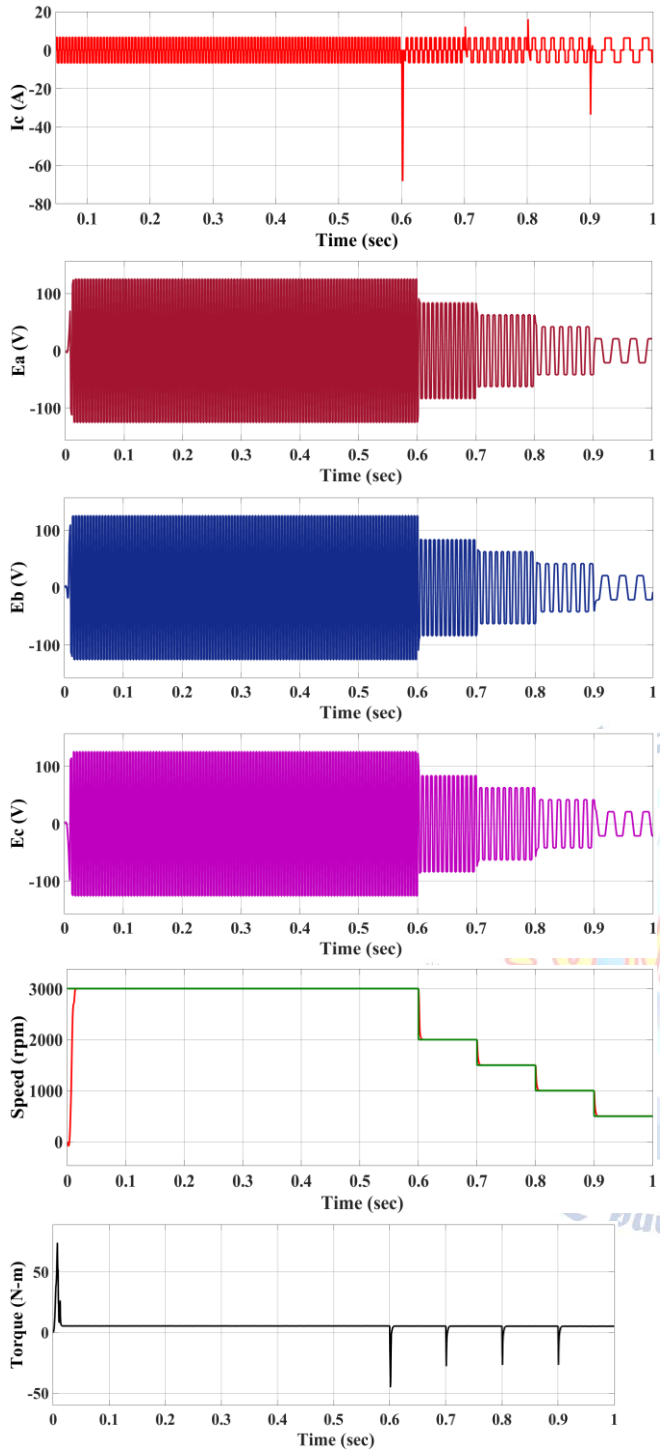

Fig.8 Simulation Results of proposed method ANN controlled BLDC motor Drive system

B. Comparative Results of PI, Fuzzy, and ANN Controllers

The comparative analysis of the PI, Fuzzy, and ANN controllers highlights clear differences in their performance under dynamic conditions as shown in Fig.9. The PI controller, being a conventional control method, shows noticeable overshoot, slower response, and longer settling time when the system is subjected to disturbances or sudden changes. It also exhibits oscillations before reaching steady state, indicating limited capability in handling nonlinear system behavior. The Fuzzy controller improves the overall system response by reducing overshoot and achieving faster stabilization. It demonstrates better adaptability to system variations and nonlinearities compared to the PI controller. The response is smoother, and the oscillations are less pronounced, making it more reliable for moderately complex systems. The ANN controller outperforms both PI and Fuzzy controllers by providing the fastest response, minimal or no overshoot, and very smooth tracking of the reference signal. It effectively handles disturbances and maintains stability with negligible oscillations. This superior performance is due to its ability to learn and adapt to system dynamics. Overall, the ANN controller offers the highest accuracy, robustness, and efficiency, followed by the Fuzzy controller, while the PI controller shows the least optimal performance among the three.

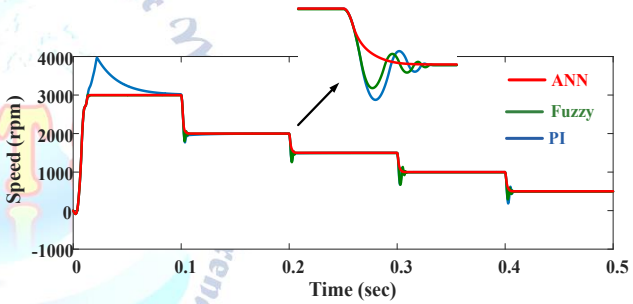

Fig.9 Simulation Results of Speed Control Using PI, Fuzzy, and ANN Controllers

V. CONCLUSION

This work presented an intelligent control approach for a solar PV integrated PMBLDC motor drive with bidirectional power flow management. The proposed system effectively combines a PV source with a P&O-based MPPT algorithm, a boost converter, and a battery energy storage system connected through a bidirectional buck–boost converter to ensure efficient energy utilization and reliable operation under varying conditions. The use of an ANN controller for speed regulation significantly enhances the overall system performance compared to conventional PI and fuzzy logic controllers. The ANN controller demonstrates superior adaptability, faster transient response, reduced overshoot, and minimal steady-state error, ensuring precise and stable motor operation even under dynamic load and environmental changes. Additionally, the

MPPT-based boost converter successfully maximizes power extraction from the PV system, while the bidirectional converter enables smooth and efficient energy exchange between the PV source, battery, and motor load. Simulation results validate that the proposed system achieves improved efficiency, better dynamic response, and enhanced stability. Furthermore, the integration of renewable energy with energy storage not only improves system reliability but also promotes sustainable and eco-friendly operation. Overall, the proposed ANN-based control scheme proves to be a highly effective solution for advanced motor drive applications in renewable energy systems.

Conflict of interest statement

Authors declare that they do not have any conflict of interest.

REFERENCES

[1] B. Saha and B. Singh, "An approach for enhanced range with regenerative braking in solar PV-battery based E-rickshaw using sensorless BLDC motor drive," in Proc. IEEE Int. Conf. Comput., Power Commun. Technol., 2020, pp. 809–814.

[2] P. Mulhall, S. M. Lukic, S. G. Wirasingha, Y.-J. Lee, and A. Emadi, "Solar/battery electric auto rickshaw three-wheeler," in Proc. IEEE Veh. Power Propulsion Conf., 2009, pp. 153–159.

[3] X. Nian, F. Peng, and H. Zhang, "Regenerative braking system of electric vehicle driven by brushlessDCmotor," IEEE Trans. Ind. Electron., vol. 61, no. 10, pp. 5798–5808, Oct. 2014,.

[4] J. W. Dixon and M. E. Ortuzar, "Ultracapacitors + DC-DC converters in regenerative braking system," IEEE Aerosp. Electron. Syst. Mag., vol. 17, no. 8, pp. 16–21, Aug. 2002.

[5] X. Zhang, Y. Wang, G. Liu, and X. Yuan, "Robust regenerative charging control based on T–S fuzzy sliding-mode approach for advanced electric vehicle," IEEE Trans. Transp. Electrific., vol. 2, no. 1, pp. 52–65, Mar. 2016.

[6] Y. Cao, T. Shi, Y. Yan, X. Li, and C. Xia, "Braking torque control strategy for brushlessDCmotor with a noninductive hybrid energy storage topology," IEEE Trans. Power Electron., vol. 35, no. 8, pp. 8417–8428, Aug. 2020.

[7] P. P. Acarnley and J. F. Watson, "Review of position-sensorless operation of brushless permanent-magnet machines," IEEE Trans. Ind. Electron., vol. 53, no. 2, pp. 352–362, Apr. 2006.

[8] K. Iizuka,H.Uzuhashi, M. Kano, T. Endo, andK.Mohri, "Microcomputer control for sensorless brushlessmotor," IEEE Trans. Ind. Appl., vol. IA-21, no. 3, pp. 595–601, May 1985.

[9] P. Damodharan and K. Vasudevan, "Sensorless brushless DC motor drive based on the zero-crossing detection of back electromotive force (EMF) from the line voltage difference," IEEE Trans. Energy Convers., vol. 25, no. 3, pp. 661–668, Sep. 2010.

[10] X. Song, B. Han, and K. Wang, "Sensorless drive of high-speed BLDC motors based on virtual third-harmonic backEMFand high-precision compensation," IEEE Trans. Power Electron., vol. 34, no. 9, pp. 8787–8796, Sep. 2019.

[11] H. Zhang and H. Li, "Fast commutation error compensation method of sensorless control for MSCMG BLDC motor with nonideal back EMF," IEEE Trans. Power Electron., vol. 36, no. 7, pp. 8044–8054, Jul. 2021.

[12] A. Sen and B. Singh, "Peak current detection starting based position sensorless control of BLDCmotor drive for PV array fed irrigation pump," IEEE Trans. Ind. Appl., vol. 57, no. 3, pp. 2569–2577, May/Jun. 2021.

[13] G. Wang et al., "Enhanced position observer using second-order generalized integrator for sensorless interior permanent magnet synchronous motor drives," IEEE Trans. Energy Convers., vol. 29, no. 2, pp. 486–495, Jun. 2014.

[14] R. Sreejith and B. Singh, "Sensorless predictive control of SPMSM-driven light EV drive using modified speed adaptive super twisting sliding mode observerwith MAF-PLL," IEEE J. Emerg. Sel. Topics Ind. Electron., vol. 2, no. 1, pp. 42–52, Jan. 2021.

[15] M. H. Bierhoff, "A general PLL-type algorithm for speed sensorless control of electrical drives," IEEE Trans. Ind. Electron., vol. 64, no. 12, pp. 9253–9260, Dec. 2017.

[16] B. Akin and M. Bhardwaj, "Sensorless trapezoidal control of BLDC motors," Texas Instruments. [Online]. Available: https://www.ti.com/lit/ an/sprabq7a/sprabq7a.pdf

[17] R. Kumar and B. Singh, "Buck-boost converter fed BLDC motor drive for solar PV array based water pumping," in Proc. IEEE Int. Conf. Power Electron., Drives Energy Syst., 2014, pp. 1–6.

[18] S. Sundeep and B. Singh, "Robust position sensorless technique for a PMBLDCmotor," IEEE Trans.Power Electron., vol. 33, no. 8, pp. 6936–6945, Aug. 2018.

[19] S. Chen, X. Zhou, G. Bai, K. Wang, and L. Zhu, "Adaptive commutation error compensation strategy based on a flux linkage function for sensorless brushless DC motor drives in a wide speed range," IEEE Trans. Power Electron., vol. 33, no. 5, pp. 3752–3764, May 2018.

[20] X. Zhou, X. Chen,M. Lu, and F. Zeng, "Rapid self-compensation method of commutation phase error for low- inductance BLDC motor," IEEE Trans. Ind. Inform., vol. 13, no. 4, pp. 1833–1842, Aug. 2017.

[21] S. Sashidhar, V. Guru Prasad Reddy, and B. G. Fernandes, "A single-stage sensorless control of a PV-based bore-well submersible BLDC motor," IEEE J. Emerg. Sel. Topics Power Electron., vol. 7, no. 2, pp. 1173–1180, Jun. 2019.

[22] "How to calculate wheel and vehicle speed from engine speed." [Online]. Available: https://x-engineer.org/automotive-engineering/chassis/ vehicle-dynamics/calculate-wheel-vehicle-speed-engine-speed/

[23] Sreejith R. and K. R. Rajagopal, "An insight into motor and battery selections for three-wheeler electric vehicle," in Proc. IEEE 1st Int. Conf. Power Electron., Intell. Control Energy Syst., 2016, pp. 1–6.

[24] Ministry of New and Renewable Energy, "Solar rooftop calculator," India. [Online]. Available: https://solarrooftop.gov.in/

[25] R. Lairenlakpam, G. D. Thakre, P.Gupta,Y. Singh, and P.Kumar, "Effect of different drive modes on energy consumption of an electric auto rickshaw," in Proc. IEEE Transp. Electrific. Conf., 2017, pp. 1–5.